Revisiting an Enigma on California's North Coast: The M_w 6.5 Fickle Hill Earthquake of 21 December 1954

Margaret Hellweg*[1], Thomas A. Lee[2,3], Douglas S. Dreger[4], Anthony Lomax[5], Lijam Hagos[6], Hamid Haddadi[6], Robert C. McPherson[7], Lori Dengler[8], Susan E. Hough[9], and Jason R. Patton[10]

ABSTRACT

Many earthquakes occur along the North Coast of California in the vicinity of the Mendocino Triple Junction (MTJ), where the Pacific, Gorda, and North American (NA) plates meet, and on the adjacent plate boundaries. The MTJ marks the nexus of the Mendocino and San Andreas faults with the Cascadia subduction zone (CSZ). Historically, most large earthquakes around the MTJ have been within the offshore Gorda plate and its subducted portion beneath the NA plate. North of the MTJ, active faults mapped in the NA plate are part of the CSZ fold-and-thrust belt. Although some events have been detected in the NA plate, no large historic events have been associated with mapped surface faults. The 21 December 1954 M_w 6.5 earthquake in Humboldt County is one possible exception. Using published data from catalogs and articles, unpublished data from Berkeley's archives, and *S-P* times interpreted from two U.S. Coast and Geodetic Survey (USCGS) accelerometers, we determine a probability cloud for the earthquake's hypocenter using NonLinLoc. The highest probability location lies beneath Fickle Hill just east of the city of Arcata, California, at 40.87° N, 124.03° W, and ~11 km depth. Using *P*-wave polarities from Berkeley stations and the digitized waveforms from the accelerometers, we find that the focal mechanism most consistent with the data indicates thrust movement with strike, dip, and rake of 350°, 10°, and 90°, respectively, at a depth of 14 km. Given the depth uncertainties of both this event and the megathrust, this implies that the earthquake most likely took place on the subduction interface rather than on the mapped faults in the Mad River fault zone that trend 322° and dip to the northeast. The revisited intensity in the epicentral region also supports a location beneath Fickle Hill to the east of the city of Arcata, California.

KEY POINTS

- The source fault of the 21 December 1954 M_w 6.5 earthquake has remained a puzzle even after 70 yr.
- Seismic evidence and models suggest that the 1954 earthquake occurred on the Cascadia subduction interface.
- Revisiting predigital earthquakes, as shown in this study, can increase our understanding of tectonics and hazard.

Supplemental Material

INTRODUCTION

On 21 December 1954, just before noon local time, an earthquake with magnitude 6.5 shook communities on the North Coast of California surrounding Humboldt Bay (Roberts and Cloud, 1958; Murphy and Cloud, 1984). The shaking in Arcata, California, Eureka, California, and nearby areas was much stronger than that of the frequently occurring large earthquakes near the Mendocino Triple Junction (MTJ) or in the Gorda Plate offshore and caused much damage (Steinbrugge and Moran, 1957; Roberts and Cloud, 1958; Murphy and Cloud, 1984;

1. Berkeley Seismology Laboratory, University of California Berkeley (Retired), Orinda, California, U.S.A.; 2. Department of Geosciences, Princeton University, Princeton, New Jersey, U.S.A., https://orcid.org/0000-0002-0227-8239 (TAL); 3. Geology Department, University of Hawaii, Hilo, Hawaii, U.S.A.; 4. Berkeley Seismology Laboratory (Retired), Earth and Planetary Science, University of California Berkeley, Berkeley, California, U.S.A., https://orcid.org/0000-0002-6590-3089 (DSD); 5. Anthony Lomax Scientific Software, Mouans-Sartoux, France, https://orcid.org/0000-0002-7747-5990 (AL); 6. California Geological Survey, Strong Motion Instrumentation Program, Sacramento, California, U.S.A., https://orcid.org/0000-0002-7061-2147 (HH); 7. Geology Department, California Polytechnic Humboldt (Retired), Bayside, California, U.S.A., https://orcid.org/0009-0009-4189-7735 (RCMP); 8. Geology Department, Cal Poly Humboldt, Arcata, California, U.S.A.; 9. U.S. Geological Survey, Earthquake Hazards Program, Pasadena, California, U.S.A., https://orcid.org/0000-0002-5980-2986 (SEH); 10. California Geological Survey, Seismic Hazards Mapping Program, Tsunami Unit, Arcata, California, U.S.A., https://orcid.org/0000-0003-3657-5490 (JRP)

*Corresponding author: hellweg@berkeley.edu

Cite this article as Hellweg, M., T. A. Lee, D. S. Dreger, A. Lomax, L. Hagos, H. Haddadi, R. C. McPherson, L. Dengler, S. E. Hough, and J. R. Patton (2025). Revisiting an Enigma on California's North Coast: The M_w 6.5 Fickle Hill Earthquake of 21 December 1954, *Bull. Seismol. Soc. Am.* **XX**, 1–17, doi: 10.1785/0120250080

Hough *et al.*, 2025). This earthquake has been referred to in the literature by several names. In this study, based on the preferred location obtained herein, we refer to it as the Fickle Hill earthquake.

Seismicity in the region was not unexpected by the residents of Humboldt County, at least since the early 1900s; the 1906 Great San Francisco earthquake was felt strongly in the area (Dengler *et al.*, 1992; Toppozada and Barnum, 2004). The region, where three tectonic plates meet, is among the most seismically active in California. The nexuses of these plates, the Pacific, Gorda, and North American (NA), are the Mendocino and San Andreas faults and the Cascadia subduction zone (CSZ). Additional seismic hazard stems from the many active faults mapped in the NA plate, which are interpreted as part of the CSZ fold-and-thrust belt (Kelsey and Carver, 1988; Clark and Carver, 1992). As we now know, the majority of large earthquakes around the MTJ have taken place within the Gorda plate offshore and in its subducted portion beneath the NA plate and along the Mendocino fault. Although some events have been detected in the NA plate north of the MTJ, no large historic events have been clearly associated with the mapped surface faults.

The possible exception to the dearth of large earthquakes in the NA plate is the 21 December 1954 M_w 6.5 earthquake. The location and seismotectonics of this event remain enigmatic, as it occurred before the present era of broadly available, digital seismic data. The earthquake was well recorded for the time, including two nearby triggered accelerometers and other stations of the U.S. Coast and Geodetic Survey (USCGS), on seismographs operated by the Berkeley Seismographic Stations (BSS, now the Berkeley Seismology Laboratory [BSL]) of the University of California Berkeley, and the California Seismological Laboratory (CSL) at the California Institute of Technology in Pasadena, California, as well as at other regional and teleseismic sites. Locations of the earthquake (Fig. 1) determined in the years following 1954 include those of the BSS (Milne, 1957), the USCGS (1954b), the International Seismological Centre (ISC) (2025), as well as a thesis (Tocher, 1956a); several articles that used the earthquake to study "False S" (Cameron, 1961a,b), and a report from the 1970s to understand the seismic hazard related to the Humboldt Nuclear Power Plant (Tenekron Energy Resource Analysts [TERA], 1977). No focal mechanism was ever reported for this event, and with the exception of TERA (1977), none of the reported locations included a depth for the earthquake.

The purpose of this study is to collect the available data about the earthquake and use modern methods and seismic velocity models to determine an improved hypocentral location including depth, calculate a moment magnitude, if possible, and estimate the event's focal mechanism. We also revisit the intensity distribution, based on the detailed felt and damage reports collected by the USCGS (Roberts and Cloud, 1958; Murphy and Cloud, 1984; Hough *et al.*, 2025), as well as newspaper archives, recently discovered photos, detailed maps of the water supply pipeline for Eureka, which broke in the earthquake, and recently collected eyewitness accounts (see the supplemental material, available to this article, for the contents of the Assembled Data Set and Data and Resources). The goal is to discover whether the earthquake occurred within the mantle of the subducting Gorda plate, on the Cascadia subduction interface, or whether it is associated with a mapped surface fault within the NA plate.

AVAILABLE DATA AND RESOURCES

There are a variety of sources of original data relating to the 1954 Fickle Hill earthquake. The original records from the BSS stations operating at the time, as well as the original reading sheets for the event, are still present at the BSL (see Data and Resources). The reading sheets also include picks from the seismic stations operated by the CSL. The USCGS operated seismic stations in the western United States included a "weak motion" station at Ukiah, California, and two triggered accelerometer stations in the epicentral area at Eureka, California, and Ferndale, California (EUR and FER; Cloud, 1965). Finally, global arrivals from the event are reported in the 1954 annual Bulletin of the ISC ((2025) as well as more recently on the ISC website (ISC, 2025). Cameron (1961a) gave *S-P* times, t_{S-P}, determined from aftershocks at the BSS stations. This abundance of information, for example, the arrival picks available in the various catalogs and bulletins and their polarities, as well as the three-component waveforms from the two accelerometer stations, has not previously been collected to support a thorough analysis of the Fickle Hill earthquake. We apply current methods and regional velocity models to these data to update the determination of its hypocenter and to determine its focal mechanism. A complete compendium of local, regional, and global arrivals for the Fickle Hill earthquake is available at the ISC (2025), but the location given there is based on a global solution.

SEISMIC RECORDS

The BSS operated 11 seismic stations (Table S1) at the time of the Fickle Hill earthquake. We were able to find and scan the records from nine of the stations; the records of the mainshock from COR could not be located in the archive, and the records from SHS are on 35 mm film, the readability of which is limited due to equipment constraints. The closest station to the earthquake was ARC (Figs. 1, 2). The collected records were scanned at 1200 pixels per inch (ppi) in 24 bit three-channel color with a Contex IQ 4400 scanner and with an original digital format of TIFF that was later converted to JPG. The physical records typically measure approximately 100 cm in length and usually have either 15 or 30 min of data recorded on each trace. With a typical length of about 45,000 horizontal pixels, the effective resolution of the scanned data is either 50 or 25 pixels per second for 15 or 30 min traces, respectively (see Data and

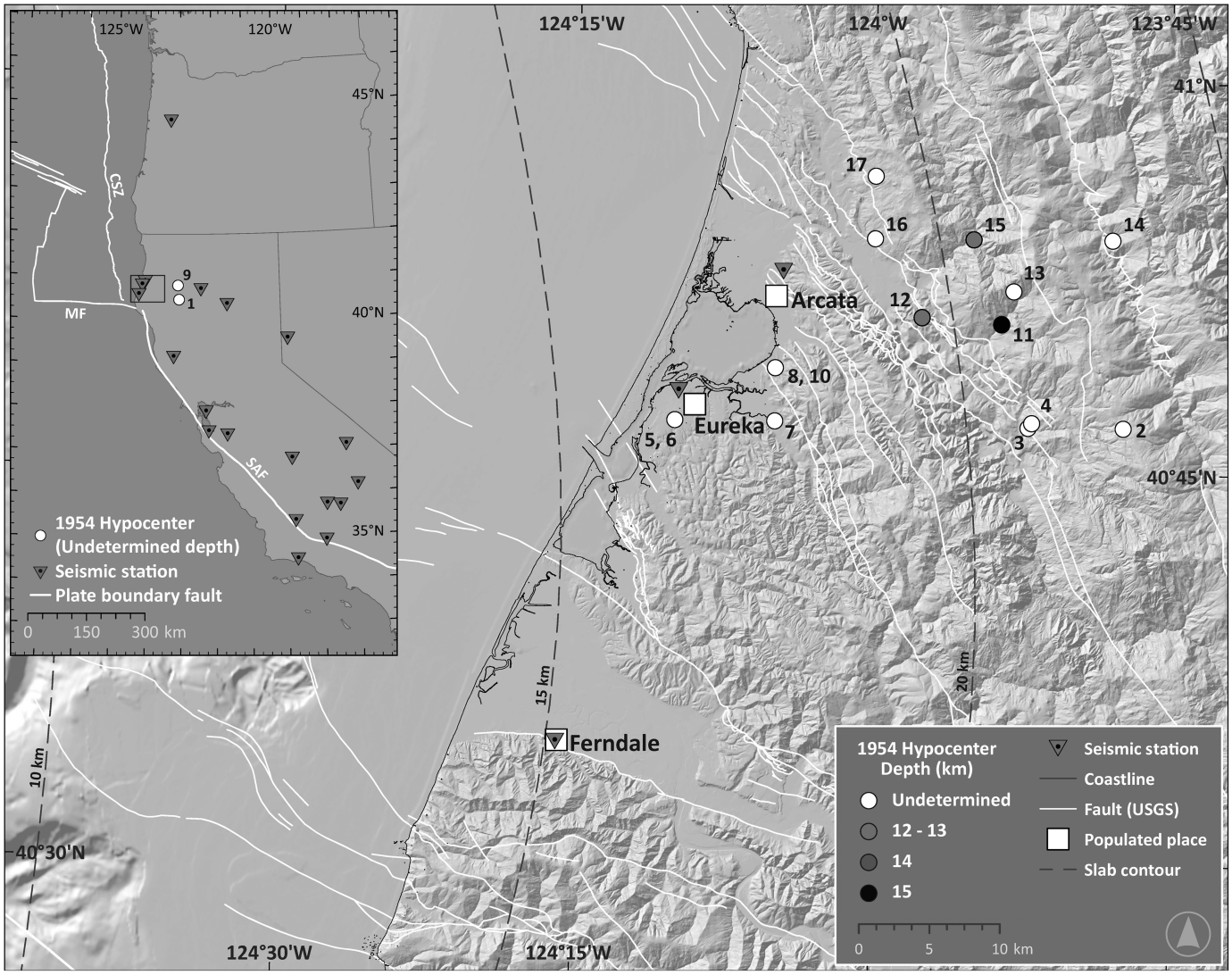

Resources). In addition to the records from the mainshock, we collected and scanned the records available for the largest aftershock, M_w 4.7, which occurred on 30 December 1954 at 09:16:13 UTC. This latter set includes records for the Z and E components at COR as well as at several other BSS stations. Table S1 includes information on the stations' locations, the equipment operating at the time (Bolt and Miller, 1975), and whether the records were found and scanned.

Our primary use of the scanned BSS records is to read the polarity of the *P* arrival (Table 1) for use in determining the focal mechanism, because most of the nearby stations went off-scale immediately following the *P* arrival (see, e.g., Fig. 2c), although we also include the arrival times used in the analysis for determination of the location. For the purpose of determining the polarities, we assume that the orientations of the sensors given on the records are correct. In addition, for ARC and FER, where only horizontal records are available for the *P* arrival, we infer the vertical polarity (Table 1) of the arrival from the horizontal records (Plešinger *et al.*, 1986). We also infer the polarity of the *P* arrival for MIN from the horizontals,

Figure 1. Historical hypocenters (numbered circles) and seismic stations (inverted triangles) used in the study. The inset shows an overview of the region including the plate boundary faults (San Andreas [SAF], Mendocino [MF], and Cascadia subduction zone [CSZ]; Coffin *et al.*, 1998), with the zoomed area indicated by the box. The stations used in the study are in California, Nevada, and Oregon (Table 1, see also the supplemental material) and are operated by the University of California's Berkeley Seismographic Stations, the California Seismological Laboratory at the California Institute of Technology, and the U.S. Coast and Geodetic Survey. The two easternmost historical locations for the 21 December 1954 earthquake are shown on the inset map (white circles). The main map shows a view of the hypocentral region, including mapped faults in the North American (NA) plate (white lines; USGS and CGS, 2025), the locations of the cities of Arcata, Eureka, and Ferndale (white squares), and the locations of the three seismic stations nearest the event, ARC, EUR, and FER (inverted gray triangles). The contours of the 15 and 20 km depths of the CSZ slab from the Slab2 model (Hayes *et al.*, 2018) are shown as dashed lines. Historical hypocenters are also shown (circles), with circles in different gray shades indicating those that include an estimate of event depth. The numbers indicate which organization or person calculated the location and the reference that documents each hypocenter (see the supplemental material). Onshore elevation information is from United States Geological Survey (USGS) (2009) and offshore depths are from Ryan *et al.* (2009).

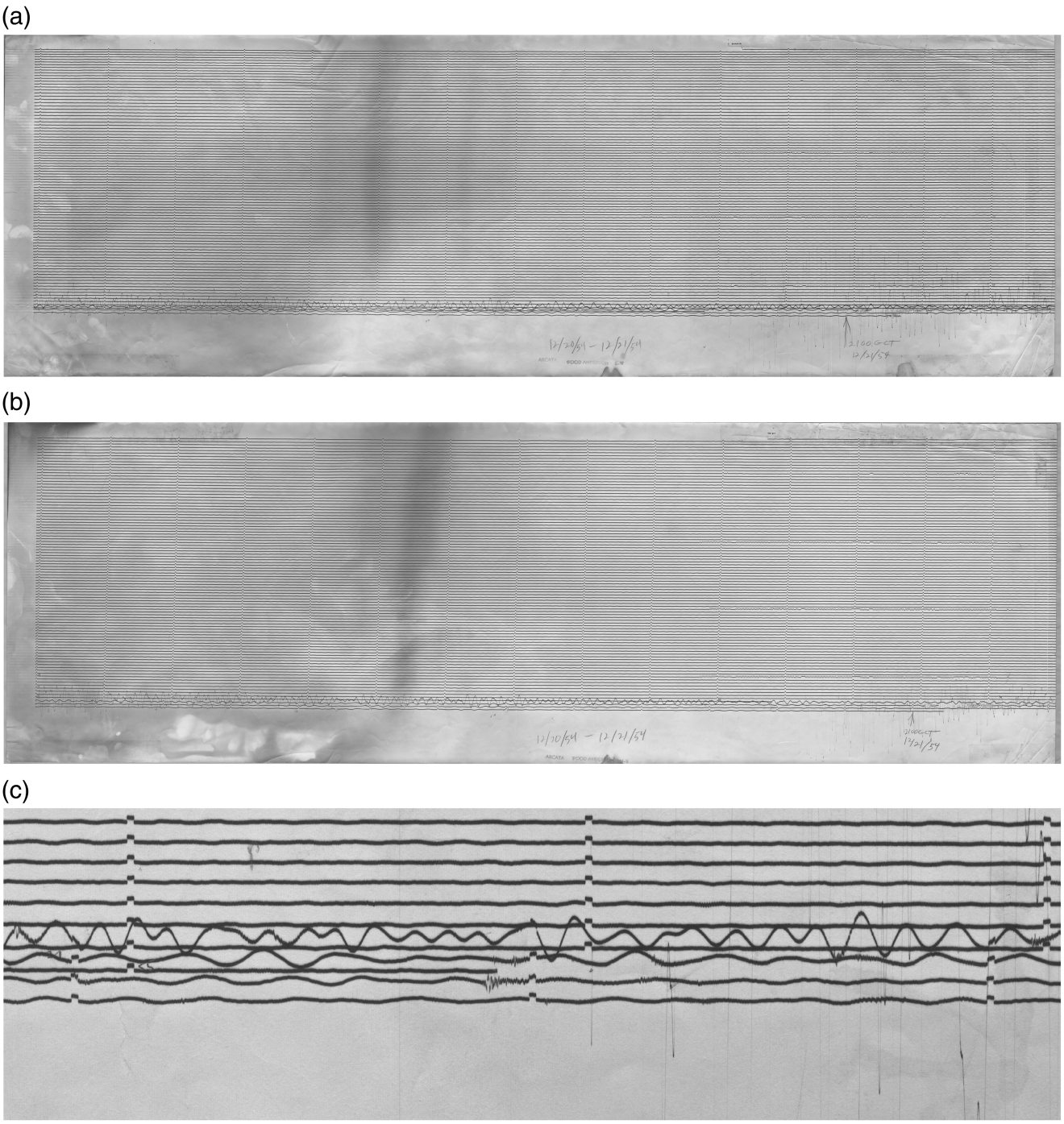

as the arrival on the vertical Benioff channel is not clear due to noise. Finally, we assume that the vertical polarity observed for the *P* wave of the largest aftershock at COR is the same as it would have been for the mainshock.

As we began work on the Fickle Hill earthquake, we were pleased and surprised to receive paper copies of the recordings for the event from triggered accelerometers (L. Gee, U.S. Geological Survey, oral personal communication, February 2022) of the type USCGS Strong Motion Seismograph (Cloud, 1965) operated by the USCGS in Eureka (EUR) and

Figure 2. Records from the station ARC, located in Arcata, California, on the grounds of and operated collaboratively with what was then Humboldt State College (now Cal Poly Humboldt). (a) Record of the east–west-oriented Wood–Anderson (WA) seismograph starting at 20:55 UTC on 20 December 1954. (b) Record of the north–south-oriented WA seismograph starting at 20:55 UTC on 20 December 1954. (c) First onset from ARC-EW. Note that on both records between the onset of the Fickle Hill earthquake and the time the light rays were slow enough to be recorded on the paper again, their position relative to the recording drums changed. This can be seen because after the onset, the minute marks are no longer aligned, and several of the traces overlap the previous traces, as is apparent in the blowup of the ARC-EW record, as well as in the full records of the east–west and north–south seismometers discussed earlier. This may have been due to power failure and/or shifts in the instrumentation.

TABLE 1
Phase Arrivals Including Polarities and Source Information for the Polarity of the *P* Phases

Station	Phase	Abs. Time*	Arrival Time (hh:mm:ss.s)	Uncert (s)†	Prior Wt‡	Pred TT (s)§	Resid(s)‖	Post Wt#	Distance (km)	Azimuth (°)	*P*-Polarity MS V	*P*-Polarity MS N	*P*-Polarity MS E	*P*-Polarity AS V	*P*-Polarity AS N	*P*-Polarity AS E	Polarity Source
ARC	*P*	Y	19:56:31.7	1.0	1	2.5	0.1	1.8	3.9	285	+	–	–		–	–	V inferred, N and E record
ARC	*S*	N	19:56:34.2	2.0	0	4.5	0.6	0.0	3.9	285							
EUR	*P*	N	19:56:33.0	1.0	1	3.6	0.5	0.2	13.4	236							
EUR	*S*	N	19:56:36.3	2.0	1	6.5	0.0	0.1	13.4	236							
FER	*P*	Y	19:56:39.0	1.0	1	7.6	0.6	0.1	37.9	211	+	–	–				V inferred, N and E reading
FER	*S*	N	19:56:45.5	2.0	1	13.5	0.0	0.1	37.9	211							
SHS	*P*	Y	19:56:50.4	1.0	1	21.3	0.1	1.5	139.9	97	+						Reading sheet
SHS	*S*	Y	19:57:07.6	2.0	1	38.0	0.5	1.2	139.9	97							
UKI	*P*	Y	19:56:58.0	1.0	1	29.4	–0.5	1.4	205.1	160							
UKI	*S*	Y	19:57:16.0	1.0	1	52.4	–5.5	0.2	205.1	160							
MIN	*P*	Y	19:56:59.5	1.0	1	30.9	–0.5	1.4	213.3	105	+	+	+				V inferred, S and E reading sheet
MIN	*S*	Y	19:57:24.0	2.0	1	55.0	–0.1	1.2	213.3	105							
BRK	*P*	Y	19:57:18.4	1.0	1	49.6	–0.3	1.4	366.6	155	+	–	+				Records
BRK	*S*	Y	19:57:59.7	2.0	1	88.3	2.3	0.8	366.6	155							
REN	*P*	Y	19:57:22.7	1.0	1	52.7	0.9	1.3	387.9	111	+	–	+	–	+	+	Records
PAC	*P*	Y	19:57:24.6	1.0	1	55.8	–0.3	1.4	416.1	157	+	–	+				Records
PAC	*S*	Y	19:58:08.0	2.0	1	99.3	–0.4	1.0	416.1	157							
COR	*P*	Y	19:57:26.0	1.0	1	56.1	0.8	1.3	418.1	8				+		–	Records
COR	*S*	Y	19:58:07.8	2.0	1	99.8	–1.1	1.0	418.1	8							
MHC	*P*	Y	19:57:28.4	1.0	1	59.6	–0.3	1.4	443.5	151	+	+	+	+			Records
MHC	*S*	Y	19:58:15.3	2.0	1	106.1	0.1	1.0	443.5	151							
FRE	*P*	Y	19:57:47.1	1.0	1	77.0	1.0	1.2	585.7	140	+	+	+	+	+	+	Records
TIN	*P*	Y	19:57:50.0	1.0	1	86.3	–5.4	0.3	657.4	128							
KRC	*P*	Y	19:58:03.2	1.0	1	94.2	–0.1	1.2	722.0	147							
WDY	*P*	Y	19:58:03.4	1.0	1	95.4	–1.1	1.1	732.2	140							
HAI	*P*	Y	19:58:08.0	1.0	1	97.5	1.4	1.1	746.9	133							
ISA	*P*	Y	19:58:08.5	1.0	1	98.5	0.9	1.1	755.8	138							
FTC	*P*	Y	19:58:13.9	1.0	1	104.7	0.1	1.2	805.3	144							
SBC	*P*	Y	19:58:15.5	1.0	1	105.1	1.3	1.1	810.1	150							

E, east; N, north; S, south; and V, vertical.
*Abs time: Absolute time—whether the arrival time is directly from picks on the record or inferred (see text).
†Uncert: Assigned uncertainty at the beginning of analysis.
‡Prior Wt: Assigned weight at the beginning of analysis.
§Pred TT: Travel time predicted for the most likely location.
‖Resid: Residual between measured arrival and predicted arrival times.
#Post Wt: Weight assigned by the algorithm for the most likely solution.

Ferndale (FER, Fig. 3). It appears that these copies were made as part of the effort to digitize the accelerograms in 1969 (Hudson, 1969). The equipment in Ferndale was collocated with the BSS seismographs in the Ferndale City Hall, and the instrument in Eureka was sited in the Eureka Federal Building (now the Eureka Post Office). Information for these strong-motion seismographs, including their orientations, is also given in Table S1. This equipment triggers when the ground motion becomes strong enough to close the electric contacts of the pendulum starter. The recording on light-

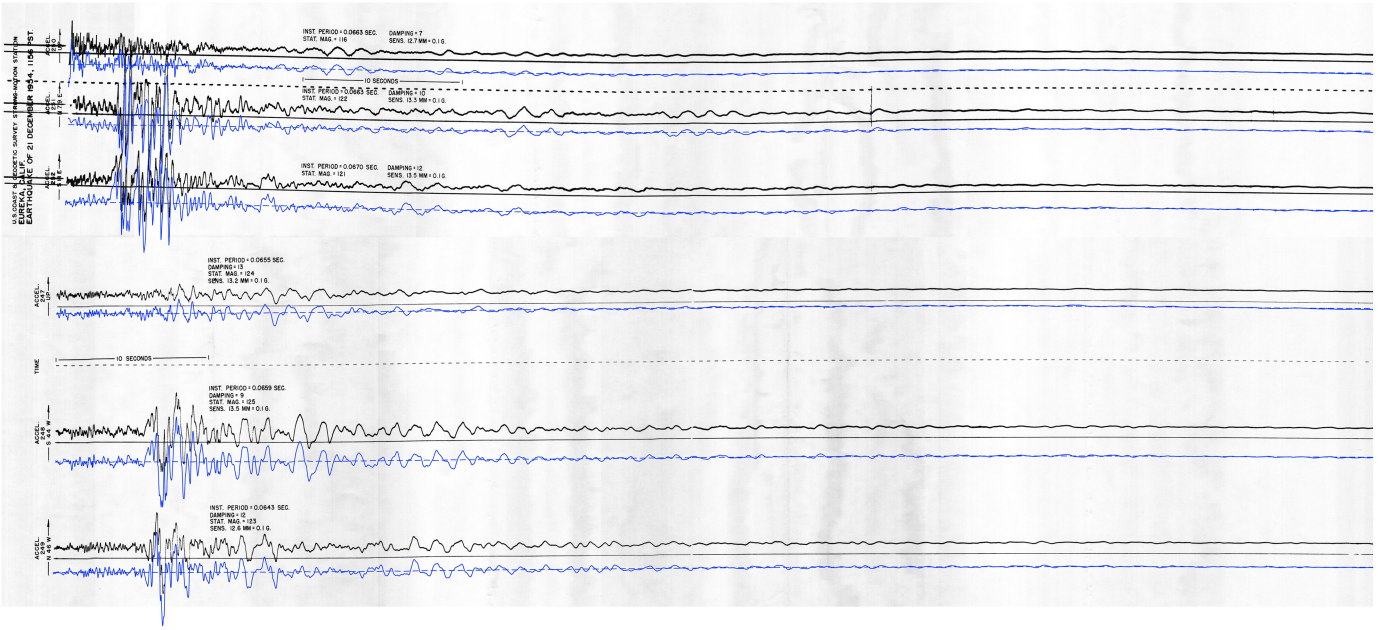

Figure 3. Scans of paper three-component accelerograms from (top) EUR and (bottom) FER. Blue traces show the digitized coordinates of the waveforms and are offset down for ease of comparison to the original paper records. The color version of this figure is available only in the electronic edition.

sensitive paper includes both timing marks from a clock mechanism and three components of ground motion (vertical, lateral, and transverse to the orientation of the unit). The triggering time for the strong-motion seismograph is given as a graph in Cloud (1965). For this analysis, we assume that the instruments trigger on the arrival of the *P* wave and that the beginning of the record is 0.5 s after the *P* arrival. These records provide two important contributions for our study. The first is that they are close to the earthquake, and they give us an assumed value for t_{S-P}. For FER, we assume that the *P* arrival reported for the BSS seismographs also triggered the USCGS accelerometer, although we have no absolute *P*-arrival time for EUR. The second is that we also have near-complete on-scale waveforms from these two stations close to the epicenter, which we can use to estimate the moment magnitude and evaluate possible focal mechanisms for the earthquake. All records from other nearby BSS stations, particularly the closest station to the earthquake, ARC (Fig. 2), immediately go off-scale with the arrival of the *P* wave.

To make the data from EUR and FER accessible to modern techniques, we have scanned and digitized these three-component strong-motion records. The paper copies of the records were scanned using a Contex IQ 4400 scanner to create digital copies with a resolution of 1200 dpi and 24 bit color in JPEG format. These records were then analyzed using the DigitSeis tool (Ishii and Ishii, 2022) to extract the accelerogram traces in Cartesian (*x*, *y*) coordinates. This output format was necessary due to the lack of helicorder-style minute marks in the individual traces used to assign timing in the DigitSeis software.

Although timing could be assigned by linear interpolation between the given start and end times of the record, this was avoided due to the possibility of distortion of the paper and its copy in the *x*-direction (Lee *et al.*, 2022). To minimize timing uncertainty in the record, the presence of time marks, which are formatted as horizontal dashes and gaps representing 0.25 s in time across the length of the record, is leveraged. Particularly, the number of pixels equivalent to an elapsed time of 0.25 s is logged as a function of horizontal position throughout the record (Fig. 4). This measurement of equivalence between time and pixels is smoothed with a rolling average and utilized to convert the Cartesian coordinates to *y*-position in pixels as a function of time in seconds. The start time for the trace given on the original record is used to determine absolute time for the data (Fig. 4). In addition, a rolling average is used to smooth the *y*-position coordinate and determine a zero line from which amplitude in pixels can be measured. Having generated time series from the scanned images, the data have been converted into the widely used SAC format and are available along with the original scans as part of the assembled data set at the Northern California Earthquake Data Center (NCEDC) (see Data and Resources).

PHASE ARRIVALS

Phase arrivals for the Fickle Hill earthquake are reported in the Bulletin of the BSS (Milne, 1957) as well as the Bulletins of the USCGS (1954b) and the ISC (2025). Rather than using the BSS Bulletin, we retrieved the reading sheets for the event and used the arrivals reported there, including timing corrections for each station. These scans are available as part of the assembled data set at the NCEDC (see Data and Resources). For example, for ARC, the timing correction is given as +43.2 s. The reading sheets also reported arrivals from CSL stations. In total, we

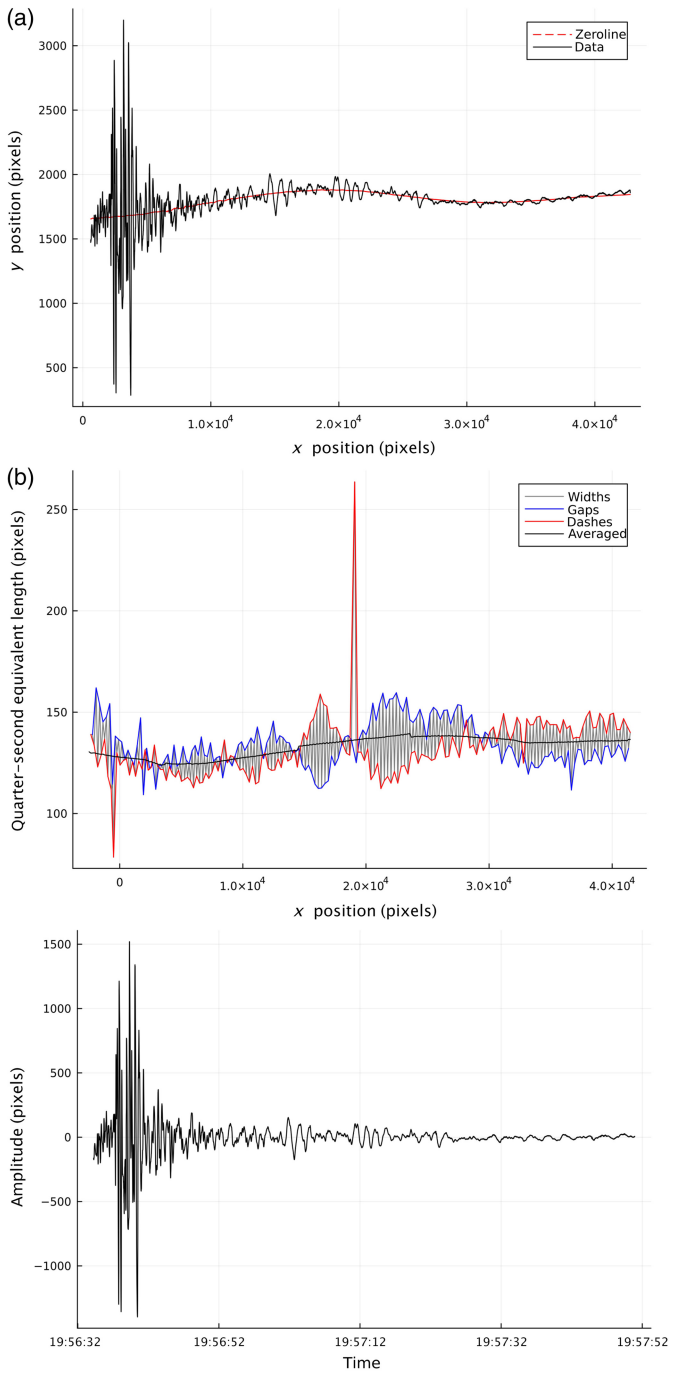

Figure 4. The processing of the digitized trace for the N79° E component of motion at EUR. (a) Trace in Cartesian (*x*- and *y*-position) coordinates as extracted from scans (black) and the zero line determined using a rolling average (dashed red). (b) The width of one-quarter second measured in pixels used to assign timing to the traces; values for all widths (gray), gaps (blue), dashes (red), and their rolling average (blue) are given as a function of the *x*-position on the scan. (c) The trace given as amplitude as a function of time after subtraction of the zero line and time assignment. The color version of this figure is available only in the electronic edition.

found arrivals for 19 stations. In all cases, we assumed that the corrections for the arrival times related to the separation of the "timing source" from the recorder have been properly applied

TABLE 2
Smooth Velocity Model Derived from Henstock and Levander (2003) and the MEN2 Model Derived from Oppenheimer, Klein, *et al.* (1993)

Top Depth (km)	V_P (km/s)	V_P Gradient ([km/s]/km)	V_S (km/s)	V_S Gradient ([km/s]/km)
−5.00	2.92	0.000	1.64	0.000
0.00	2.92	0.422	1.64	0.237
4.10	4.64	0.238	2.61	0.133
10.00	6.05	0.095	3.40	0.053
20.00	7.00	0.333	3.93	0.187
23.00	8.00	0.000	4.49	0.000

and that all stations use the same time base. The set of stations we used for the analysis and the phase arrival times are given in Table 1 and Table S1, respectively. The set of phase arrivals used to relocate the earthquake includes the inferred t_{S-P} from the accelerometer records at EUR and FER, which provide important constraints for the hypocentral distance. For ARC, estimates of t_{S-P} for the mainshock range from 2.0 to 2.9 s with an average of 2.5 s are based on the values observed for aftershocks in the time following the mainshock (Cameron, 1961a; TERA, 1977). We also use t_{S-P} given by Cameron (1961a) for SHS, MIN, and COR, based on the observations of aftershock phase arrivals. Other *S*-arrival times are given in the BSS reading sheets and for UKI in the USCGS Bulletin (1954b).

RELOCATION

In the literature, 14 epicenters are given for the Fickle Hill earthquake, clustering between 40.78° N and 124.17° W in the southwest and 40.94° N and 124.0° W in the northeast (Fig. 1). In the printed USCGS report for 1954 (USCGS, 1954b; Roberts and Cloud, 1958; Murphy and Cloud, 1984), three different locations are given, although one of them appears to be a typographic error. The other epicenters stem from the BSS Bulletin for 1954 (Milne, 1957); several locations from the ISC, including the original location in the 1954 Bulletin (2025), Tocher's doctoral thesis (1956a), and Cameron (1961a).

To ensure that the hypocenter of the relocated Fickle Hill earthquake is consistent with current locations for northern California seismicity reported by the Northern California Seismic System, we use only the regional arrivals to a hypocentral distance of about 810 km—those for the BSS and CSL stations, and the Ukiah, California (UKI), station of the USCGS—for a total of 19 stations (Table 1 and Table S1). We use a smooth *P*-wave velocity model (Table 2 and Fig. S2) derived from the mean of slowness with depth from two models for the Mendocino area: a representative depth profile from Henstock and Levander (2003) and the MEN2 model from Oppenheimer, Klein, *et al.* (1993). Such a smooth model avoids location artifacts at layer interfaces. The uncertainties for *P* and *S* arrivals are set to

±1 and ±2 s, respectively. For EUR, which does not have absolute timing, only the t_{S-P} difference is used to constrain the location. For FER, we use the *P*-arrival time from the BSS equipment and t_{S-P} from the collocated USCGS accelerometer.

We relocate the 1954 event applying the NonLinLoc (NLL) algorithm (Lomax *et al.*, 2000, 2014) to a 200 km × 200 km area centered on latitude 40.4°, longitude −124.4°, with test depths ranging from 0 to 40 km. This algorithm requires a large suite of travel times from each station to the test hypocenters within the model space. To calculate the *P* travel times, we use a finite-difference, eikonal-equation algorithm (Podvin and Lecomte, 1991) and divide these values by a constant $V_P/V_S = 1.78$ to calculate *S* travel times. The travel time uncertainty along each path is assumed to be 2% of the calculated travel time, with minimum and maximum permitted values of 0.05 and 2.0 s, respectively. This effectively performs distance weighting related to the length of each path.

The NLL algorithm (Lomax *et al.*, 2000, 2014) uses efficient global sampling algorithms to obtain an estimate of the posterior probability density function (PDF) in 3D space for the absolute hypocentral location. This sampling uses the octree cascading grid search (Lomax *et al.*, 2014), so the finest scale grid spacing is very small relative to the search volume and the uncertainties in the location. For example, at the depth of location with the highest probability and at the other tested depths, the spacing of the search grid was ∼300 m. The location PDF provides a complete description of likely hypocentral locations and includes comprehensive uncertainty information. Within NLL, we use the equal differential-time (EDT) likelihood function (Zhou, 1994; Font *et al.*, 2004; Lomax, 2005, 2008; Lomax *et al.*, 2014), which is very robust in the presence of outlier data caused by large errors in the arrival-time picks. The robustness of the EDT likelihood is important for this study of the 1954 event, because outlier picks are frequent in phase data from the instrumental period before the 1960s due to timing problems and other challenges, such as difficulties in picking phases on paper or other analog records (Adams, 2004).

Figure 5 shows the cloud of probable locations and their relationship to the three closest stations, ARC, EUR, and FER. The hypocentral solution with the highest probability, the "most likely" location, is at 40.87° N, 124.03° W, and at a depth of ∼11 km, with horizontal and vertical uncertainties of ±12.3 and ±15.1 km, respectively (Fig. 5). This is just 3.9 km east-southeast of the station ARC in the city of Arcata, California, beneath Fickle Hill, both a community east-southeast of Arcata and the name of a hill. The Fickle Hill fault in the NA plate, part of the Mad River fault zone, transects the hill from southeast to northwest, with an approximate trend of 322° (United States Geological Survey and California Geological Survey [USGS and CGS], 2025).

The densest part of the PDF of possible locations (Fig. 5, red dots) describes an east–west-trending ellipsoid, which is shallower in the east and deeper as it approaches ARC. The t_{S-P} values from the accelerometer records from EUR and FER and their uncertainties contribute important constraints to the PDF. The east–west trend and the north–south width of the PDF essentially describe an arc centered on FER and defined by the uncertainty in its t_{S-P} value. The east to west dip is controlled by the t_{S-P} value from EUR, which defines the maximum probable hypocentral distance $\sqrt{h^2 + d^2}$, in which h is the hypocentral depth and d is the epicentral distance. Thus, if the hypocenter is more distant from EUR, then it must be shallower. Conversely, if the hypocenter is closer to EUR, it must be deeper. The length of the ellipsoid in the east–west direction is also determined by t_{S-P} at EUR. Both the most likely hypocenter and the trend of the probability ellipsoid are consistent with t_{S-P} observed from the aftershocks recorded at ARC (Cameron, 1961a; TERA, 1977). Indeed, if we include $t_{S-P} = 2.5$ s for ARC given in Cameron (1961a), in calculating the hypocenter, the cloud of possible locations (red dots) tightens considerably, but the most likely solution does not change. Overall, the shape and location of the probability cloud depend strongly on the velocity model, the quality and distribution of phase picks, as well as the location algorithm and the specific settings of other parameters, such as the uncertainty assigned to the arrival times. This means that the cloud generally favors a depth of ≤20 km for the event and an epicenter along a west–east-trending patch within ∼10 km of ARC. It is difficult to say more, because of trade-offs and uncertainties in the various parameters. An NLL solution for the hypocenter determined using only the information from the nearest three stations, ARC, EUR, and FER, exhibits the same trends as the overall solution, with the exception that the cloud of probabilities is slightly less dense than the solution presented earlier and lies slightly more to the north.

FOCAL MECHANISM, MAGNITUDE, AND STRESS DROP

To determine a focal mechanism for the Fickle Hill earthquake, two types of data are available; the observed and inferred polarities of the first onsets from the records of the BSS stations and the waveforms from the two USCGS accelerometer stations, which do not include the *P* arrival. For the former, only the polarities are available, and for most stations the trace on the light-sensitive paper disappears almost immediately because the light tracking the onset was moving so quickly. The polarity is only visible by carefully examining the record, especially by magnifying the section of the record with the first onset (Fig. 2c). In the case of four stations, ARC, FER, MIN, and COR, we have inferred the vertical polarity, as described earlier, based either on the horizontal records or for the last, based on the record of the largest aftershock.

To determine the probable focal mechanism, we need to evaluate the possible locations as a function of depth due to the east–west deepening trend in the hypocentral locations. Thus, for each of the fixed test depths to be used in the search for the focal mechanism (1.5, 3.5, 5.5, 8, 11, 14, 18, 21, 24, 27,

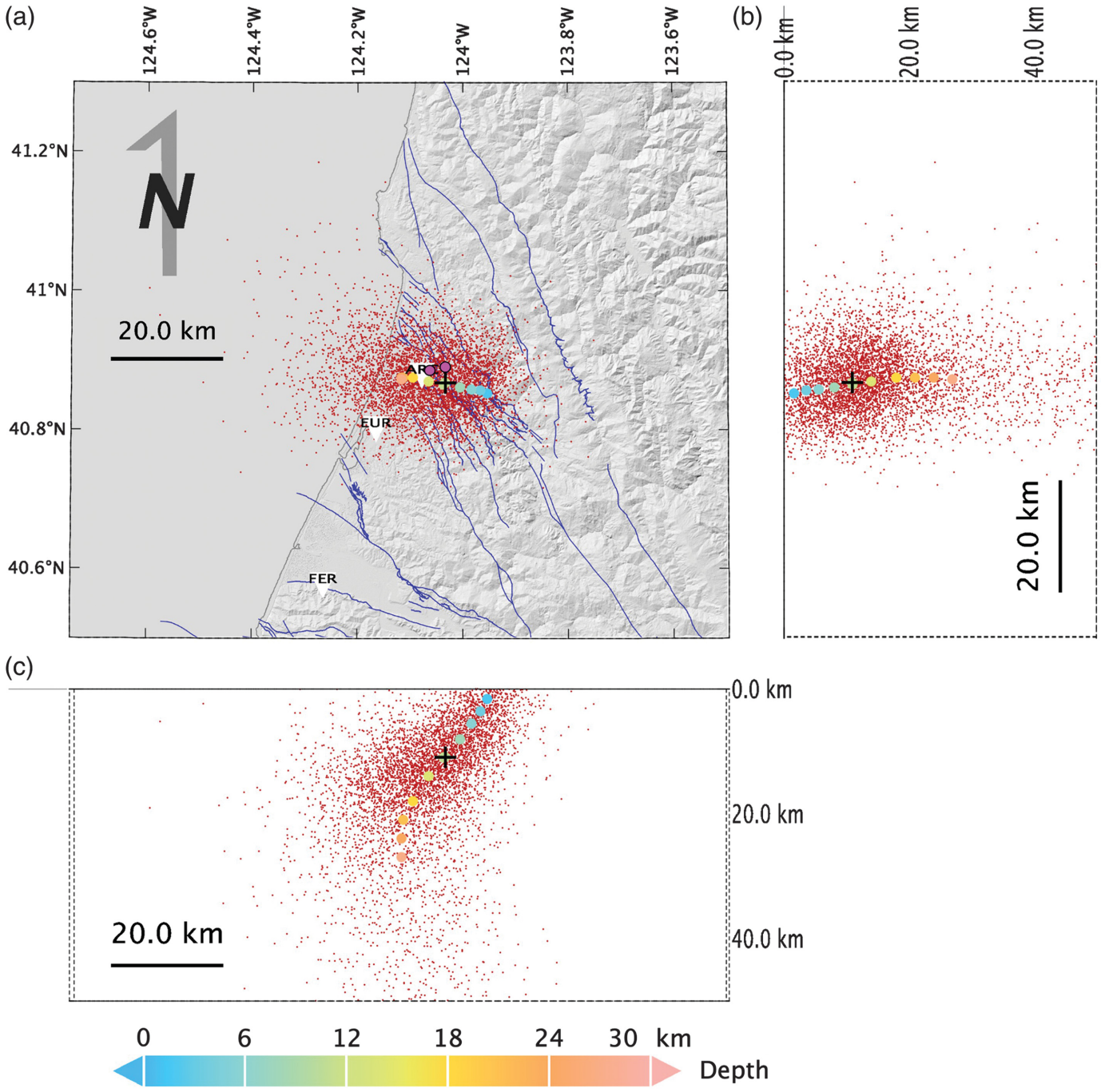

and 30 km), we calculated the most likely hypocentral location (Table 3) and the concomitant azimuths and take-off angles for each of the stations. The latitudes of the most likely hypocentral locations at all of the test depths (Table 3) lie to the south of the latitude of the closest station ARC, 40.878°. Hypocenters to the southeast of ARC are inconsistent with its horizontal *P*-wave vector, which has negative onsets on both horizontal channels (Plešinger *et al.*, 1986). Source locations consistent with this observation must lie either to the southwest of ARC, and the vertical *P*-arrival would be negative, or to the northeast of ARC, in which case the vertical *P* arrival would be positive (Plešinger *et al.*, 1986).

Figure 5. Probability of likely hypocentral locations for the M_w 6.5 Fickle Hill earthquake determined using the NonLinLoc method (Lomax *et al.*, 2000, 2014). Views from (a) above (center), (b) east (right), and (c) south. The locations of the three nearest stations, ARC, EUR, and FER, are shown as inverted triangles. In all three views, the most likely location is shown by the + sign, and the dots show most likely locations at depths of 1.5, 3.5, 5, 8, 11, 14, 18, 21, 24, 27, and 30 km. These locations are all to the east-southeast of the station ARC. The magenta dots show likely hypocenters to the east-northeast of ARC at depths of 11 and 14 km, respectively. Dark lines represent the mapped faults in the NA plate (see Data and Resources).

TABLE 3
Best Locations at Test Depths

Direction from ARC	Latitude	Longitude	Depth (km)	Horizontal Uncertainty (km)
Southeast	40.853	−123.953	1.6	9.4
Southeast	40.857	−123.966	3.6	7.4
Southeast	40.858	−123.982	5.6	7.7
Southeast	40.861	−124.005	8.1	7.1
Southeast	40.865	−124.036	11	7.6
Southeast	40.870	−124.064	14	7.1
Southwest	40.875	−124.094	18	7.6
Southwest	40.875	−124.112	21	8.4
Southwest	40.875	−124.116	24	8.1
Southwest	40.873	−124.116	27	8.8
Southwest	40.870	−124.112	30	8.4
Northeast	40.888	−124.040	11	n/a
Northeast	40.882	−124.065	14	n/a

Using the most probable hypocentral location for each test depth (Table 3 and Fig. 5), we first examine the polarities (Table 1). In particular, for the stations ARC and FER, which only have horizontal sensors, and for MIN where the vertical record is very noisy, we infer the polarity of the vertical onset of the *P* wave based on the location of the preferred hypocenter at each depth using the horizontal vector of the *P* wave (Plešinger *et al.*, 1986). As the distance to FER is on the order of 40 km, the azimuth does not change very much for the various test hypocenters. However, for ARC, which is much closer, the azimuth does change. All of the most likely test hypocenters (Fig. 5 and Table 3) lie slightly south of the latitude of ARC and get deeper as they pass from east to west. We have chosen to add two test locations to the northeast of ARC at approximately the same distances and depths as the southeast test locations at 11 and 14 km depth, because only the hypocenters located to the west of ARC are consistent with the negative polarities observed on both its N and E channels. The ARC polarity for these two sites will be positive. These two points lie slightly north of a line trending N70° E from ARC. We selected these positions, as the arctan of the first motions observed in many of the aftershocks suggested sources at varying distances lying between N60° E and N70° E of ARC. These two test hypocenters are consistent with the most probable region of the cloud of hypocenters determined using only the *P* arrivals and *S*-*P* times for ARC, EUR, and FER. The two closest stations with polarities, ARC and FER, have upgoing takeoff angles for all the test hypocenters, whereas the takeoff angles for all other stations have downgoing values.

The observed and inferred first-motion polarities are not consistent with a strike-slip focal mechanism at any depth, such as would be expected if the event had taken place within the Gorda plate, such as the earthquakes of December 2021 and 2022 (Fig. 6b and Fig. S2; Yeck *et al.*, 2023; Guo *et al.*, 2024; Hellweg *et al.*, 2024; Shelly *et al.*, 2024; Yoon and Shelly, 2024), or on a theoretical nearby fault with movement such as that observed along the Mendocino fault (Fig. 6c and Fig. S2).

We estimate the focal mechanism and scalar seismic moment of the event using a forward-modeling approach in which local and regional distance vertical-component *P*-wave polarities are fitted simultaneously with the three-component accelerometer waveforms recorded at the stations EUR and FER. The data from these latter two stations were digitized and instrument corrected as previously described. For the determination of the focal mechanism, the acceleration records were integrated to ground velocity. Velocity Green's functions were calculated using the GIL7 velocity model (Table 3 and Fig. S3; Dreger and Romanowicz, 1994) using the Herrmann (2013) FK-integration program. The GIL7 velocity model is appropriate for the region and is used for routine moment tensor estimation at the BSL (e.g., Romanowicz *et al.*, 1993; Pasyanos *et al.*, 1996). Synthetic seismograms were computed from the Green's functions. The first step was to convolve them with a trapezoidal source time function with a rise time of 0.05, a high time of 0.7, and a decay time of 0.5 s. Then, the strike, dip, rake, and scalar moment source parameters were iteratively adjusted and the corresponding fits inspected. The data and synthetics were both bandpass filtered between 0.1 and 0.5 Hz using an acausal four-pole Butterworth filter. The trapezoidal source time function is needed to account for the source duration at these two close stations, and the trapezoidal source time function parameters were adjusted by forward modeling to best fit the waveshape in the modeled passband.

Figure 6a shows the most convincing results in which a north–south-striking, low-angle reverse focal mechanism for the source to the northeast of ARC at 14 km depth satisfies both the first-motion polarity data and the three-component waveforms for EUR and FER reasonably well. The source parameters are strike/dip/rake = 350°/10°/90° and a scalar moment of 5×10^{18} N · m ($M_w = 6.4$). The moment magnitude is consistent with $M_L = 6.5$ determined in 1954 by the BSS. The depth of 14 km can be considered to be the depth of the main moment release or the slip centroid.

This determination of the focal mechanism is not well constrained given the sparse data, and it is not possible to formally assess the uncertainties. To illustrate that the data preferentially support this low angle focal mechanism, we compare its fit to examples of the more typical strike-slip focal mechanisms observed in the area, a west–east-striking "Mendocino fault" and a northeast–southwest-striking Gorda intraplate fault (Fig. 6b,c; see the supplemental material; Yeck *et al.*, 2023; Hellweg *et al.*, 2024; Shelly *et al.*, 2024; Yoon and Shelly, 2024). We also show an example for the fits to a thrust focal mechanism consistent with the Fickle Hill fault mapped in the NAP (Fig. 6d and Fig. S1). This fault has a strike trending at 322° and steeper dip than the best-fitting focal mechanism. Note also that the positive polarity at FER lies outside the compressional region of the focal mechanism, and the fits

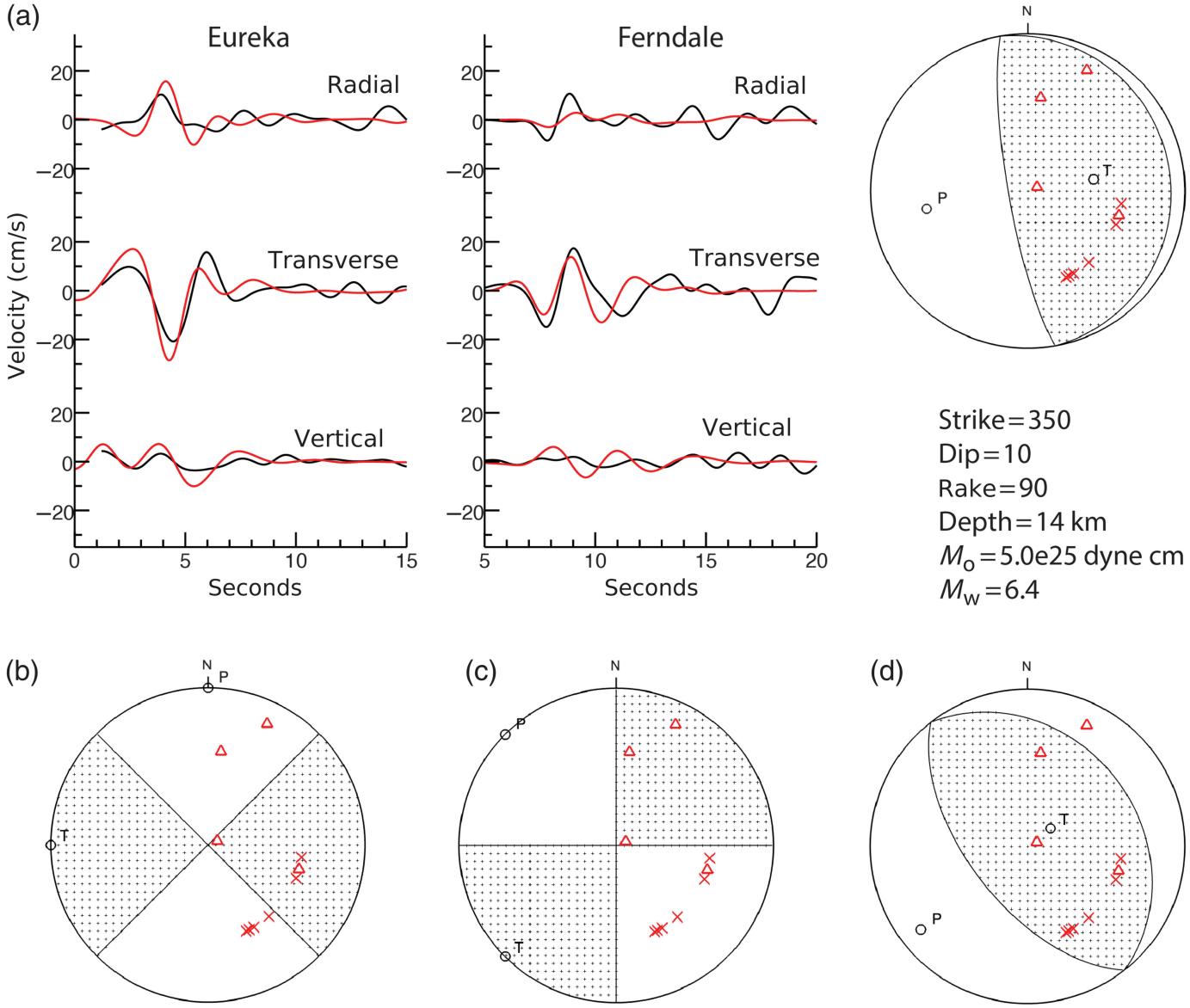

Figure 6. (a) Mechanism for the 1954 event for a centroid of release at a depth of 14 km to the northeast of the station ARC. (Left) Observed (black) and synthetic (red) waveforms at Eureka (EUR) and Ferndale (FER) have a good level of fit in the 0.1–0.5 Hz passband. (Right) The best-fit mechanism showing observed and inferred *P*-wave polarities. Red symbols denote up first motion and green down (no down first motions are observed in this case). "X" shows polarities directly observed on vertical components, whereas triangles show vertical polarities inferred from the observation of the two horizontal *P*-wave polarities. The circles indicate the P and T axes. (b–d) Sample mechanisms for the same hypocentral location for mechanisms typical of a Gorda intraplate event, an MF fault event, and an event on the Fickle Hill fault or one of the other faults in the NA plate, respectively. The symbol key is the same as for (a). Waveform fits for EUR and FER for these mechanisms are shown in the supplemental material.

to the waveforms at EUR and FER are not as good as those in Figure 6a.

Finally, we estimate the stress drop for the Fickle Hill earthquake using the transverse component velocity spectra derived from the records at EUR and FER (Fig. 7, black lines). The basis for the analysis is again broadband Green's functions generated using the GIL7 velocity model. From them, we estimate the spectrum of an average focal mechanism (red lines) by sweeping through the mechanism space and using the spectral shape of Boatwright (1980). The modeling reveals a high-frequency fall-off exponent of 2.8 and corner frequencies of 0.69 and 0.69 Hz for EUR and FER, respectively (Fig. 7). These corner frequencies are consistent with the short duration of the primary *S*-wave pulse observed in both the velocity and displacement records. From this analysis, the moments for the stations EUR and FER are 3.3×10^{18} N · m and 6.9×10^{18} N · m, respectively. These moments bracket the value from the mechanism fitting. It is noted that FER can be better fit with a higher moment, but we capped it at M_w 6.5 based on the other magnitude estimates. There are likely unaccounted for site effects at the higher frequencies used to the spectral fitting. Assuming a directivity model using fault dimensions from Leonard (2010), we

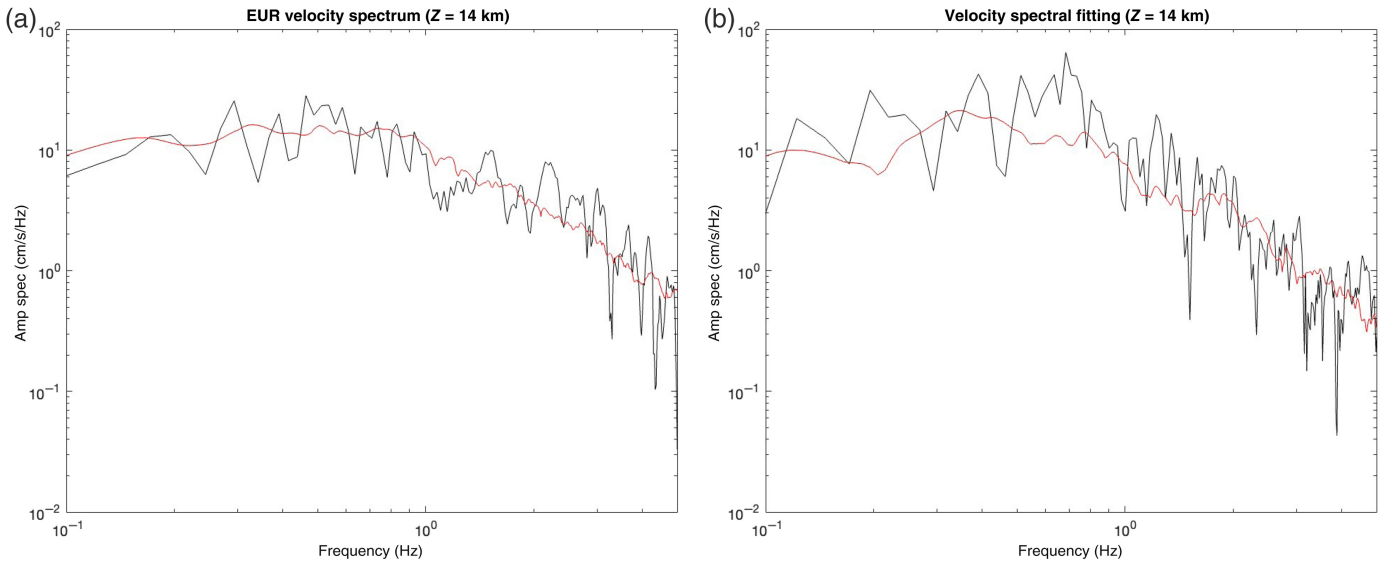

Figure 7. Spectral fits for stress-drop analysis for the waveforms from (a) EUR and (b) FER. Black lines show the velocity spectra determined from the integrated accelerograms of the transverse motion at each site. Red lines are the best-fit Boatwright (1980) spectrum. See the Focal Mechanism, Magnitude, and Stress Drop section for detailed explanation. The color version of this figure is available only in the electronic edition.

calculated a directivity correction factor relating the observed corner frequency to that expected for a perpendicular observation of the rupture. This reduces corner frequencies by factors of 0.357. The resulting Brune stress drops are 6.5 MPa for EUR and 13.5 MPa for FER. These raw stress drops are high owing to the very short widths of the *S*-wave pulses and the corner frequencies, which are high for an earthquake with $M_w \sim 6.5$. It is noted that there is considerable uncertainty in the corner frequency and therefore stress drop owing to site effects, which are not accounted for, the assumed directivity correction, and the moment scaling of the spectra. Although the data are too sparse to uniquely determine the rupture plane, the east-northeast-dipping plane is the most probable rupture plane in that a rupture toward the southwest and updip toward EUR and FER could explain the short duration of the *S*-wave pulses and the high measured corner frequencies. The more steeply dipping plane does not allow rupture toward those stations.

MACROSEISMIC DATA

At the time of the 1954 earthquake, the USCGS collected macroseismic data using postcards, typically left at Post Offices (Byerly and Dyk, 1936). These data were summarized in the United States Earthquakes publication series (see Data and Resources). More complete summaries were presented in a preliminary, lesser-known report series: "Abstracts of Earthquake Reports for the Pacific Coast and Western Mountain Region" (hereinafter the Abstract Series). For the Fickle Hill earthquake, USCGS (1954a) included reports from over 500 locations, including 130 locations where shaking was reportedly not felt, and dozens of reports from the cities of Eureka and Arcata and their environs with street addresses included. With respect to spatial sampling at the ZIP-code scale, the volume and completeness of this dataset rivals modern "Did You Feel It?" data (Dengler and Dewey, 1998; Wald *et al.*, 1999) from the region.

Previously published macroseismic data are presented in a readily accessible format and discussed in detail by Hough *et al.* (2025), including newly interpreted intensities using the modified Mercalli intensity (MMI) scale (Richter, 1958). Interpreted intensities are close to values assigned by USCGS (1954a), differing on average by less than ¼ unit. To obtain preferred intensity values, intensity assignments are averaged with original USCGS (1954a) values.

Based on the standard intensity questionnaire, with dense spatial sampling, the resulting set of intensities is far more complete and reliable than intensities gleaned from media accounts, with the usual tendency of media reports to focus on the most dramatic effects (Hough, 2013). However, media and eyewitness accounts can provide important additional information from the near-field region. In an ongoing parallel effort, we (LD) have collected accounts from individuals who experienced and remembered the earthquake and these are included in our characterization of near-field intensities.

Finally, the intensity distribution includes instrumental intensity values estimated from the triggered strong motion recordings from EUR and FER. We follow the standard ShakeMap recipe, estimating MMI 7.0 and 6.6 at Eureka and Ferndale, respectively. These values are slightly higher than, but generally consistent with, the average values inferred from the USCGS (1954a) reports. We use the intensity distribution to generate ShakeMaps (Fig. 8), again following standard modern conventions (Worden *et al.*, 2020). The intensity distribution confirms the instrumental results in several ways. First, although accounts are concentrated in the larger cities near the coast (Eureka, Arcata, and Ferndale), the strongest documented shaking was east of Arcata, supporting the hypocentral location under Fickle Hill. Second, although

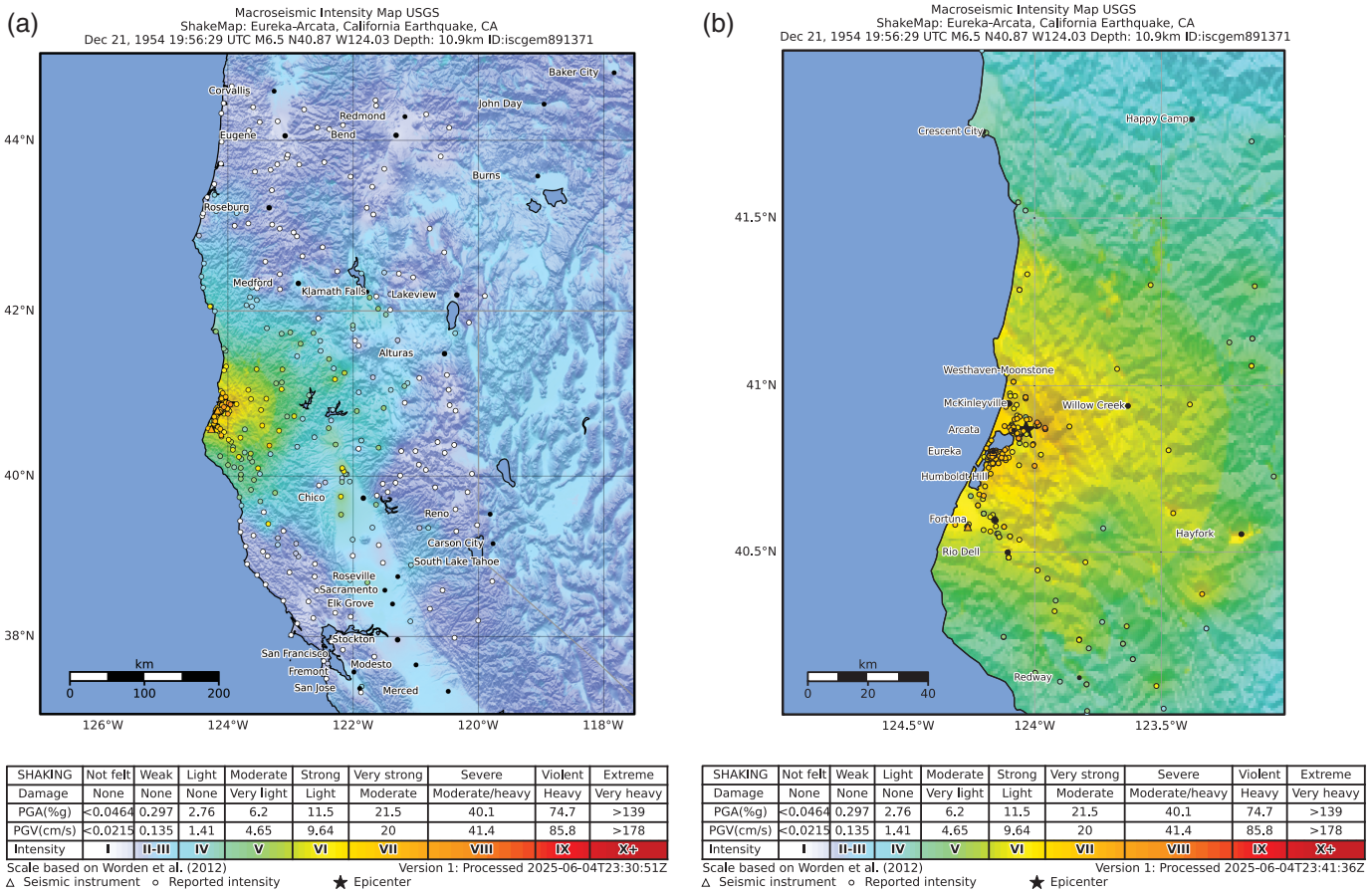

SHAKING	Not felt	Weak	Light	Moderate	Strong	Very strong	Severe	Violent	Extreme
Damage	None	None	None	Very light	Light	Moderate	Moderate/heavy	Heavy	Very heavy
PGA(%g)	<0.0464	0.297	2.76	6.2	11.5	21.5	40.1	74.7	>139
PGV(cm/s)	<0.0215	0.135	1.41	4.65	9.64	20	41.4	85.8	>178
Intensity	I	II-III	IV	V	VI	VII	VIII	IX	X+

Scale based on Worden et al. (2012) Version 1: Processed 2025-06-04T23:30:51Z
△ Seismic instrument ○ Reported intensity ★ Epicenter

SHAKING	Not felt	Weak	Light	Moderate	Strong	Very strong	Severe	Violent	Extreme
Damage	None	None	None	Very light	Light	Moderate	Moderate/heavy	Heavy	Very heavy
PGA(%g)	<0.0464	0.297	2.76	6.2	11.5	21.5	40.1	74.7	>139
PGV(cm/s)	<0.0215	0.135	1.41	4.65	9.64	20	41.4	85.8	>178
Intensity	I	II-III	IV	V	VI	VII	VIII	IX	X+

Scale based on Worden et al. (2012) Version 1: Processed 2025-06-04T23:41:36Z
△ Seismic instrument ○ Reported intensity ★ Epicenter

Figure 8. (a) Regional and (b) zoomed in reevaluated shaking intensity for the 1954 Fickle Hill earthquake (Hough *et al.*, 2025) using the current ShakeMap approach based on ground-motion models and site response terms (Worden *et al.*, 2020).

shaking throughout the region was strong enough to damage masonry chimneys, the strongest documented shaking implies MMI 8 to perhaps 8.5. The paucity of higher intensities is consistent with a depth of moment release around 14 km, with intensities providing weak evidence for a somewhat deeper depth (Hough *et al.*, 2025). The intensity distribution is consistent with expectations for M_w 7.0, supporting the observed higher than average stress drop (Hough *et al.*, 2025), although source directivity may also be a factor. A striking number of accounts specifically note that shaking felt especially "rapid." This suggests relatively strong high-frequency energy and is likely to be a consequence of the very short observed *S*-wave pulses at EUR and FER, the higher than average stress drops modeled from those stations and the onshore location, which puts the event much closer to, indeed beneath, the population centers than would the offshore Mendocino fault and Gorda intraplate events commonly felt in the area.

SOURCE MECHANISM AND STRESS DROP

In the years since the scientific community has begun to better understand the complex tectonics of the MTJ and the region, the Fickle Hill earthquake has remained an enigma (Dengler *et al.*, 1992). Although there is a consensus that it occurred onshore, insufficient analysis had been done to determine its source fault. Two important pieces of information have been missing, the hypocentral depth of the event and its focal mechanism. In our reanalysis of the event, two factors suggest that the hypocenter is not within the subducting Gorda plate or its mantle. First, the event's probable depth is too shallow; the subduction interface in the area lies between 15 and 20 km below the surface, dipping from west to east (Hayes *et al.*, 2018). The uncertainties in the depths, whether it is of the most likely hypocenter at 11 km or the moment release at 14 km, are large. However, they suggest that the earthquake is more likely to lie at or above this interface. Second, given the distribution of observed positive polarities of the *P* onsets at the regional stations, a strike-slip focal mechanism, similar to those commonly observed in the Gorda events, is extremely unlikely. Rather, the 1954 Fickle Hill earthquake was determined to be a thrust event. To demonstrate that typical strike-slip focal mechanisms from the region do not satisfy the data, we prescribe the focal mechanism to approximately match that of the 20 December 2022 mainshock (Hellweg *et al.*, 2024) or some other theoretical nearby fault with the orientation of the Mendocino fault. Clearly, neither the *P*-wave polarities nor the waveforms are fit (Fig. 6b,c and the supplemental material).

Excluding the possibility of an intraplate Gorda event leaves two possible sources: A reverse fault associated with the mapped NA plate faults or a shallow east-dipping thrust fault associated with the subduction interface. Choices for the NA plate fault could be any fault in the Mad River fault zone to the east of Arcata, including the Fickle Hill fault. These faults all trend northwest–southeast at approximately 322° and dip to the northeast (USGS and CGS, 2025). The "elephant in the room" fault is the Cascadia subduction interface. Its strike is close to north–south, and it dips at about 11° to the east in this area (Hayes *et al.*, 2018).

Let us consider the suite of most likely locations at the test depths determined through NLL analysis (colored dots in Fig. 5). All these locations lie to the southeast and southwest of the station ARC. The locations to the southeast are at depths shallower than 14 km but are inconsistent with the observed polarities of the *P* arrival on the N and E horizontal sensors at ARC (Plešinger *et al.*, 1986). For the locations to the southwest, the depths are 18 km and greater. For these locations, however, the inferred polarity for the vertical motion at ARC would be the only negative first motion (see the supplemental material, Plešinger *et al.*, 1986) among all the observations. Nonetheless, the focal mechanisms that fit both the polarities and the waveforms at the test depths of 18 and 21 km best are also north–south-striking thrust faults with shallow dip to the east (see the supplemental material). These locations are quite deep, however, at or below the region of dense hypocenter probability. This, along with the inferred negative vertical polarity for ARC is concerning, and arguably inconsistent with the distribution of other polarities and any focal mechanism considering the complete distribution of polarity data.

The range of likely hypocenters in the dense region of the probability cloud is relatively broad and includes space to the northeast of ARC. Thus, we chose to explore sources in this quadrant, at depths of 11 and 14 km close to the most likely hypocenter. For the chosen locations, approximately N70° E of ARC, the best-fitting focal mechanisms also exhibit the strike and dip of the Cascadia subduction interface. For solutions at both depths, all the observed and inferred *P*-wave polarities are consistent with the focal mechanism, and the waveform fits are reasonable (Fig. 6, see the supplemental material). We find the fits slightly better for the 14 km depth than for 11 km as well as better agreement between the moment magnitude and the BSS reported M_L.

We considered the Fickle Hill fault, or one of the other Mad River fault zone members, as a possible source for this earthquake, with a strike of 322° and a dip of 30°. The fits to the waveforms from EUR and FER are not as good as for the north–south striking and shallowly dipping solution (see the supplemental material). However, the big discrepancy is that the inferred vertical polarity for the *P* arrival at FER is not consistent with the focal mechanism. An argument similar to that made for ARC and the shifting of the test hypocenters location is not valid, as the change in the azimuth from the event to FER is only very small for all of the test hypocenters used in the focal mechanism analysis, so any choice of hypocenters from the region of likely sources would still exhibit the same inconsistency.

Thus, we conclude that the Fickle Hill earthquake is most likely to have ruptured the Cascadia subduction interface. The orientation of the focal mechanism that best fits both the *P*-wave polarities and the recordings from EUR and FER (Fig. 6a) has a strike, dip, and rake of 350°, 10°, and 90°, respectively, with the centroid of release at a depth of 14 km. Interestingly, the 1992 M_w 7.2 Cape Mendocino earthquake shares at least three characteristics with the 1954 Fickle Hill event: its source mechanism, its depth, and its location at or above the decollement (Oppenheimer, Beroza, *et al.*, 1993). The 1992 event had a hypocentral depth of about 14 km and exhibited a reverse mechanism with a plane dipping shallowly to the east consistent with the megathrust. Velasco *et al.* (1994) calculated a stress drop of 90 bars. Ironically, it is still being debated whether the 1992 event was above the megathrust or in the NA plate, as details of the depth of the megathrust throughout the area are not well known. These are similar to the problems we face in understanding the Fickle Hill earthquake.

Finally, although high stress drop is more characteristic of intraslab earthquakes than plate interface events (Strasser *et al.*, 2010), a detailed investigation of the Northern Chilean subduction zone found a range of stress drop values for events along that subduction zone (Folesky *et al.*, 2023). Details of the rupture mechanism aside, the 1954 Fickle Hill earthquake represents an especially hazardous class of events for the region, with both an onshore location and a high stress drop.

CONCLUSIONS

Fourteen or more locations have been given in the literature for the Fickle Hill event of 21 December 1954 (USCGS, 1954a; Tocher, 1956a,b; Milne, 1957; Roberts and Cloud, 1958; Cameron, 1961a, 1961b; TERA, 1977; Murphy and Cloud, 1984; United States Geological Survey [USGS], Earthquake Hazards Program, 2017; ISC, 2025). With the exception of the ISC-GEM location given in ComCat (last updated on 18 October 2023 and last visited on 1 February 2025; United States Geological Survey [USGS], Earthquake Hazards Program, 2017) and at the ISC (2025), and that in the TERA (1977), these locations were mostly calculated in the 1950s with the analysis methods in use at the time and are lacking an estimate of the event's depth. The ISC-GEM location used a global velocity model and was strongly influenced by many teleseismic phases.

We present a re-examination of the extant and accessible predigital data associated with the Fickle Hill earthquake, including previously unused but high-quality accelerograms, and the application of modern methods, tectonic understanding,

and seismic velocity models. The results have contributed new insights into its source, which we conclude was likely to have been on the interface between the Cascadia and North American plates. This would make the 1954 earthquake the first large event in the instrumental era to be documented to have been on the locked boundary.

Although the precision and accuracy of analog-era seismic data is lower relative to modern data products, the cutting-edge methodologies, computational power, and data access of the period were also crude relative to modern standards. Hence, as is demonstrated here, application of modern tools and techniques to these historical data can yield new and valuable results that leverage the previously unrealized, inherent value of legacy data.

Similarly, for many U.S. earthquakes in the 1930s through the 1960s, high-quality and high-density felt and damage reports collected by the USCGS are available for reevaluation that may contribute to improving the understanding of those earthquakes. Reviews of existing information such as this study can result in improving regional tectonic insights and thereby also the estimation of hazard.

Finally, our study of the 1954 Fickle Hill earthquake provides a template for the re-examination of other significant earthquakes of the predigital age. Careful analysis of archival records and the application of modern analytic methods can reveal new insights into tectonic regimes.

DATA AND RESOURCES

Background data and archival material used in this study have been compiled and are available in an Assembled Data Set at the Northern California Earthquake Data Center (NCEDC, 2014; https://ncedc.org/pub/assembled/Fickle_Hill_1954/). This material includes scans of all collected seismograms from the event and its largest aftershocks from the BSS stations; scans of the USCGS accelerograms for EUR and FER as well as the digitized data in the form of SAC records; scans of the BSS recording sheet pages for the event; scans of the 1954 BSS Bulletin (cover page, page providing hypocenter and origin time, and the page(s) providing arrivals); scans of the ISC 1954 Bulletin pages (cover page, page providing hypocenter and origin time, and the page(s) providing arrivals); and scans of the USCGS 1954 Bulletin pages (cover page, page providing hypocenter and origin time, and the page(s) providing arrivals). It also includes a table of the new intensity information gathered from newspaper archives, damage maps, and eyewitness accounts. Digital copies of the Abstracts of Earthquake Reports series can be found online at the Hathi Trust (https://babel.hathitrust.org/cgi/pt?id=uc1.31822006834931&seq=7), a digital library that now preserves over 18 million books and other items, with the fullest access allowable by U.S. copyright law. Original macroseismic data for the 1954 earthquake are published in USCGS (1954a). The supplemental material for this article includes Figure S1 (observed [black] and synthetic [red] waveforms and first-motion observations for hypothetical earthquake focal mechanisms) and Figure S2 (a plot of the velocity models referred to in the text). Table S1 details hypocentral locations for the Fickle Hill earthquake given in the literature; Table S2 provides information about the seismic stations used in this study; and finally, Table S3 provides intensity estimates based on the reports gathered from eyewitnesses, newspapers, and other historical sources. Appendix S1 lists the resources in the Assembled Data Set at the NCEDC (https://ncedc.org/pub/assembled/Fickle_Hill_1954/). All websites were last accessed in June 2025.

DECLARATION OF COMPETING INTEREST

The authors declare that there are no conflicts of interest recorded.

ACKNOWLEDGMENTS

The authors very much appreciate the efforts of both the long-gone people who collected, published, and archived the data we have used in our analysis as well as those who continue to maintain their storage and availability. The macroseismic data have been enriched by the recent contributions of people in the region who shared their recollections or the reports passed down through their families. The authors are grateful to *BSSA* Associate Editor Richard Briggs as well as an anonymous reviewer and John Ebel for their comments that helped improve the article. The authors also thank David Oppenheimer, Shane Detweiler, Jeanne Hardebeck, and Kevin Jones for their helpful and pertinent comments provided as part of the USGS internal review process. Any use of trade, firm, or product names is for descriptive purposes only and does not imply endorsement by the U.S. Government.

REFERENCES

Adams, R. D. (2004). Re-evaluation of early instrumental earthquake locations: Methodology and examples, *Ann. Geophys.* **47,** nos. 2/3, doi: 10.4401/ag-3339.

Boatwright, J. (1980). A spectral theory for circular seismic sources: Simple estimates of source dimension, dynamic stress drop, and radiated seismic energy, *Bull. Seismol. Soc. Am.* 70**,** 1–28.

Bolt, B. A., and R. D. Miller (1975). *Catalog of Earthquakes in Northern California and Adjoining Areas, 1 January 1910–31 December 1972*, Seismographic Stations, University of California, Berkeley, 567 pp.

Byerly, P., and H. Dyk (1936). The questionnaire program for collection earthquake data, earthquake investigations in California, *US Department of Commerce Coast and Geodetic Surv. 1934-1935*, 43–48.

Cameron, J. B. (1961a). Earthquakes in the northern California coastal region (part I), *Bull. Seismol. Soc. Am.* **51,** no. 2, 203–221, doi: 10.1785/BSSA0510020203.

Cameron, J. B. (1961b). Earthquakes in the Northern California Coastal Region (Part II), *Bull. Seismol. Soc. Am.* **51,** no. 3, 337–354, doi: 10.1785/BSSA0510030337.

Clark, S. H., and G. A. Carver (1992). Late holocene tectonics and paleoseismicity, Southern Cascadia Subduction Zone, *Science* **255,** no. 5041, 188–192.

Cloud, W. K. (1965). Instruments for Earthquake Investigation p5-20, in *Earthquake Investigations in the Western United States 1931-1964*, D. S. Carder (Editor), Publication 41-2 *US Government Printing Office*, 264 pp., (Washington, D.C.: U.S. Gov. Print. Off.).

Coffin, M. F., L. M. Gahagan, and L. A. Lawver (1998). Present-day plate boundary digital data compilation, *Technical Report No. 174*, University of Texas Institute for Geophysics, 5 pp.

Dengler, L., G. Carver, and R. McPherson (1992). Sources of North Coast seismicity, *Calif. Geol.* **45,** 40–53.

Dengler, L. A., and J. W. Dewey (1998). An intensity survey of households affected by the Northridge, California, earthquake of 17 January, 1994, *Bull. Seismol. Soc. Am.* **88,** 441–462.

Dreger, D., and B. Romanowicz (1994). Source characteristics of events in the San Francisco Bay region, *U.S. Geol. Surv. Open-File Rept. 94-176*, 301–309.

Folesky, J., C. N. Pennington, J. Kummerow, and L. J. Hofman (2023). A comprehensive stress drop map from the Northern Chilean subduction zone, *J. Geophys. Res.,* doi: 10.1029/2023JB027549.

Font, Y., H. Kao, S. Lallemand, C.-S. Liu, and L.-Y. Chiao (2004). Hypocentre determination offshore of eastern Taiwan using the Maximum Intersection method, *Geophys. J. Int.* **158,** no. 2, 655–675, doi: 10.1111/j.1365-246X.2004.02317.x.

Guo, H., J. W. Atterholt, J. J. McGuire, and C. Thurber (2024). Evidence for low effective stress within the crust of the subducted Gorda plate from the 2022 December Mw 6.4 Ferndale earthquake sequence, *Seismol. Res. Lett.* **96,** 1504–1520, doi: 10.1785/0220240078.

Hayes, G. P., G. L. Moore, D. E. Portner, M. Hearne, H. Flamme, M. Furtney, and Gregory M. Smoczy (2018). Slab2, a comprehensive subduction zone geometry model, *Science* **362,** 58–61, doi: 10.1126/science.aat4723.

Hellweg, M., D. S. Dreger, A. Lomax, R. C. McPherson, and L. Dengler (2024). The 2021 and 2022 North Coast California earthquake sequences and fault complexity in the vicinity of the Mendocino Triple Junction, *Bull. Seismol. Soc. Am.* **115,** 140–162, doi: 10.1785/0120240023.

Henstock, T. J., and A. Levander (2003). Structure and seismotectonics of the Mendocino Triple Junction, California, *J. Geophys. Res.* **108,** doi: 10.1029/2001JB000902.

Herrmann, R. B. (2013). Computer programs in seismology: An evolving tool for instruction and research, *Seismol. Res. Lett.* **84,** no. 6, 1081–1088, doi: 10.1785/0220110096.

Hough, S. E. (2013). Spatial variability of "Did You Feel It?" Intensity data: Insights into sampling biases in historical earthquake intensity distributions, *Bull. Seismol. Soc. Am.* **103,** no. 5, 2767–2781, doi: 10.1785/0220110096.

Hough, S. E. (2015). Shaking from injection-induced earthquakes in the central and eastern United States, *Bull. Seismol. Soc. Am.* **104,** no. 5, 2619–2626, doi: 10.1785/0120140099.

Hough, S. E., L. Dengler, R. McPherson, L. Hagos, and M. Hellweg (2025). Did They Feel it? Legacy macroseismic data illuminations an enigmatic 20th century earthquake, *Geoscience* 134 (in press).

Hudson, D. E. (1969) Strong motion earthquake accelerograms digitized and plotted data, volume I Part A, A report on Research Conducted under a Grant from the National Science Foundation.

International Seismological Centre (2025). On-line bulletin, doi: 10.31905/D808B830.

Ishii, M., and H. Ishii (2022). DigitSeis: Software to extract time series from analogue seismograms, *Prog. Earth Planet. Sci.* **9,** 50, doi: 10.1186/s40645-022-00508-0.

Kelsey, H., and G. Carver (1988). Late Neogene and quaternary tectonics associated with the northward growth of the San Andreas Transform fault, northern California, *J. Geophys. Res.* **93,** 4797–4819.

Lee, T., M. Ishii, and P. Okubo (2022). Assessing the fidelity of seismic records from microfilm and paper media, *Seismol. Soc. Am.* **93,** 3444–3453.

Leonard, M. (2010). Earthquake fault scaling: Self-consistent relating of rupture length, width, average displacement, and moment release, *Bull. Seismol. Soc. Am.* **100,** 1971–1988, doi: 10.1785/0120090189.

Lomax, A. (2005). A reanalysis of the hypocentral location and related observations for the great 1906 California earthquake, *Bull. Seismol. Soc. Am.* **95,** no. 3, 861–877, doi: 10.1785/0120040141.

Lomax, A. (2008). Location of the focus and tectonics of the focal region of the California earthquake of 18 April 1906, *Bull. Seismol. Soc. Am.* **98,** no. 2, 846–860, doi: 10.1785/0120060405.

Lomax, A., A. Michelini, and A. Curtis (2014). Earthquake location, direct, global-search methods, in *Encyclopedia of Complexity and Systems Science*, R. A. Meyers (Editor), Springer, New York, 1–33, doi: 10.1007/978-3-642-27737-5_150-2.

Lomax, A., J. Virieux, P. Volant, and C. Berge-Thierry (2000). Probabilistic earthquake location in 3D and layered models, in *Advances in Seismic Event Location Modern Approaches in Geophysics*, C. H. Thurber and N. Rabinowitz (Editors), Vol. 18, Springer, Netherlands, 101–134, doi: 10.1007/978-94-015-9536-0_5.

Milne, W. G. (1957). Bulletin of the seismographic stations (October 1, 1954 to December 31, 1954, Vol. 24, 149–189.

Murphy, L. M., and W. K. Cloud (1984). United States earthquakes, 1954, *U.S. Geol. Surv. Open-File Rept. 84-954*, 113 pp.

NCEDC (2014). Northern California Earthquake Data Center, *UC Berkeley Seismological Laboratory*, Dataset, doi: 10.7932/NCEDC.

Oppenheimer, D., G. Beroza, G. Carver, L. Dengler, J. Eaton, L. Gee, F. Gonzalez, A. Jayko, W. Li, M. Lisowski, R. McPherson, *et al.* (1993). The Cape Mendocino, California, earthquakes of April 1992: Subduction at the Triple Junction, *Science* **261,** 433–438.

Oppenheimer, D. H., F. W. Klein, J. P. Eaton, and F. W. Lester (1993). The Northern California Seismic Network bulletin, January-December 1992, *U.S. Geol. Surv. Open-File Rept. 93-578*, doi: 10.3133/ofr93578.

Pasyanos, M. E., D. S. Dreger, and B. Romanowicz (1996). Towards real-time determination of regional moment tensors, *Bull. Seismol. Soc. Am.* **86,** 1255–1269.

Plešinger, A., M. Hellweg, and D. Seidl (1986). Interactive high-resolution polarization analysis of broad-band seismograms, *J. Geophys.* **59,** no. 1, 129–139.

Podvin, P., and I. Lecomte (1991). Finite difference computation of travel times in very contrasted velocity models: A massively parallel approach and its associated tools, *Geophys. J. Int.* **105,** no. 1, 271–284, doi: 10.1111/j.1365-246X.1991.tb03461.x.

Richter, C. F. (1958). *Elementary Seismology*, W.H. Freeman, San Francisco, 768 pp.

Roberts, E. B., and W. K. Cloud (1958). Seismological activities of the coast and geodetic survey in 1954 and 1955, *Bull. Seismol. Soc. Am.* **48,** 83–95.

Romanowicz, B. D., M. Pasyanos, and R. Urhammer (1993). Monitoring of strain release in central and Northern California using broadband data, *Geophys. Res. Lett.* **20,** 1643–1646.

Ryan, W. B. F., S. M. Carbotte, J. Coplan, S. O'Hara, A. Melkonian, R. Arko, R. A. Weissel, V. Ferrini, A. Goodwillie, F. Nitsche, *et al.*

(2009). Global Multi-Resolution Topography (GMRT) synthesis data set, *Geochem. Geophys. Geosys.* **10,** Q03014, doi: 10.1029/2008GC002332.

Shelly, D. R., D. E. Goldberg, K. Z. Materna, R. J. Skoumal, J. L. Hardebeck, C. E. Yoon, W. L. Yeck, and P. S. Earle (2024), Subduction intraslab-interface fault interactions in the 2022 Mw 6.4 Ferndale, California, earthquake sequence, *Sci. Adv.* **10,** eadl1226.

Steinbrugge, K. V., and D. F. Moran (1957). An engineering study of the Eureka, California, earthquake of December 21, 1954, *Bull. Seismol. Soc. Am.* **47,** 129–153, doi: 10.1785/BSSA0470020129.

Strasser, F. O., M. C. Arango, and J. J. Bommer (2010). Scaling of the source dimensions of interface and intraslab subduction-zone earthquakes with moment magnitude, *Seismol. Res. Lett.* **81,** no. 6, 941–950, doi: 10.1785/gssrl.81.6.941.

Tenekron Energy Resource Analysts (TERA) (1977). Tectonic significance of large historic earthquakes in the Eureka Region, 35 pp.

Tocher, D. (1956a). Seismic Velocities and Structure in Northern California and Nevada, *Doctoral Dissertation*, The University of California Berkeley, 120 pp.

Tocher, D. (1956b). Earthquakes off the north Pacific Coast of the United States, *Bull. Seismol. Soc. Am.* **46,** 165–173, doi: 10.1785/BSSA0460030165.

Toppozada, T., and D. Barnum (2004). California earthquake history, *Ann. Geophys.* **47,** 509–522.

United States Coast and Geodetic Survey (1954a). Abstracts of earthquake reports for the Pacific Coast and the Western Mountain Region, *U.S. Coast and Geodetic Survey, MSA-84*, Department of Commerce, San Francisco, California, 50–96.

United States Coast and Geodetic Survey (1954b). Seismological bulletin, *U.S. Coast and Geodetic Survey, MSA-84*, 20 pp.

United States Geological Survey (USGS) (2009) 3D Elevation Program (3DEP) 1/3 arc-second digital elevation model, available at https://www.usgs.gov/the-national-map-data-delivery (last accessed December 2009).

United States Geological Survey (USGS), Earthquake Hazards Program (2017), Advanced National Seismic System (ANSS) comprehensive catalog of earthquake events and products: Various, doi: 10.5066/F7MS3QZH.

United States Geological Survey and California Geological Survey (USGS and CGS) (2025). Quaternary fault and fold database for the United States, available at: https://www.usgs.gov/natural-hazards/earthquake-hazards/faults (last accessed March 2025).

Velasco, A., C. Ammon, and T. Lay (1994). Recent large earthquakes near Cape Mendocino and in the Gorda Plate: Broadband source time functions, Fault orientations, and Rupture complexities, *J. Geophys. Res.* **99,** no. B1, 711–728.

Wald, D. J., V. Quitoriano, L. A. Dengler, and J. W. Dewey (1999). Utilization of the internet for rapid community intensity maps, *Seismol. Res. Lett.* **70,** no. 6, 680–697.

Worden, C. B., E. M. Thompson, M. Hearne, and D. J. Wald (2020) ShakeMap manual online: Technical manual, user's guide, and software guide, doi: 10.5066/F7D21VPQ.

Yeck, W. L., D. R. Shelly, K. Z. Materna, D. E. Goldeberg, and P. S. Earle (2023), Dense geophysical observations reveal a triggered, concurrent multi-fault rupture at the Mendocino Triple Junction, *Commun. Earth Environ.* **4,** 94, doi: 10.1038/s43247-023-00752-2.

Yoon, C. E., and D. R. Shelly (2024). Distinct yet adjacent earthquake sequences near the Mendocino Triple Junction: 20 December 2021 M_w 6.1 and 6.0 Petrolia, and 20 December 2022 M_w 6.4 Ferndale, *Seism. Record* **4,** no. 1, 81–92, doi: 10.1785/0320230053.

Zhou, H.(1994). Rapid three-dimensional hypocentral determination using a master station method, *J. Geophys. Res.* **99,** no. B8, 15439, doi: 10.1029/94JB00934.

Manuscript received 7 April 2025

Queries

1. AU: Hough (2015) is not cited in the article. Please either (1) indicate that this reference entry should be deleted or (2) indicate where one or more citations should be added to the article.